

A numerical study of the transition to oscillatory flow in 3D lid-driven cubic cavity flows

Shang-Huan Chiu, Tsorng-Whay Pan, Jiwen He, Aixia Guo, and Roland Glowinski

Department of Mathematics, University of Houston, Houston, Texas, USA

Abstract: In this article, three dimensional (3D) lid-driven cubic cavity flows have been studied numerically for various values of Reynolds number (Re). The numerical solution of the Navier-Stokes equations modeling incompressible viscous fluid flow in a cubic cavity is obtained via a methodology combining a first order accurate operator-splitting, L^2 -projection Stokes solver, a wave-like equation treatment of the advection and finite element methods. The numerical results obtained for $Re=400$, 1000 , and 3200 show a good agreement with available numerical and experimental results in literature. Simulation results predict that the critical Re_{cr} for the transition from steady flow to oscillatory (a Hopf bifurcation) is somewhere in $[1870, 1875]$ for the mesh size $h = 1/96$. Via studying the flow field distortion of fluid flow at Re before and after Re_{cr} , the occurrence of the first pair of Taylor-Görtler-like vortices is connected to the flow field distortion at the transition from steady flow to oscillatory flow in 3D lid-driven cubic cavity flows for $Re < 2000$.

Key words: Driven cavity flow, Taylor-Görtler-like vortices, Navier-Stokes equations, projection method, wave-like equation method.

Classification: AMS: 65M60

1 Introduction.

Lid-driven cavity flow is a classical flow problem that has attracted attention due to its flow configuration relevant to many industrial applications, such as coating and melt-spinning processes pointed out in [1], and its importance to the basic study of fluid mechanics, including boundary layers, eddies, secondary flows, complex three-dimensional patterns, various instabilities and transition, chaotic, and turbulence, as discussed in a review paper by Shankar and Deshpande in [2]. Also it is due to its geometrical simplicity and unambiguous boundary conditions which facilitate experimental calibrations and numerical computations, thus providing an idea benchmark problem for validating numerical results and comparing results obtained from experiments and computations.

It is known that, depending on the methodologies, boundary conditions and mesh sizes used in the simulation, the critical Reynolds number (Re_{cr}) for the occurrence of the transition from a steady flow to an oscillatory flow (a Hopf bifurcation) in two-dimensional square lid-driven cavity flow varies between 8000 and 10000 (e.g., see [4], [5], [6], [7], [9] and [10]). The oscillatory instability in cubic lid-driven cavity flows has been studied recently in [11],

[12] and [13]. Numerically, Feldman and Gelfgat [11] obtained that the critical Reynolds number for the occurrence of such Hopf bifurcation is at $Re_{cr} = 1914$. Anupindi *et al.* [13] reported that their critical value is $Re_{cr} = 2300$ (but it was obtained with regularized boundary conditions). Both are more precise than a much earlier result predicted by Iwatsu *et al.*, who gave the range between 2000 and 3000 for the critical Reynolds number in [3]. Experimentally, Liberzon *et al.* [12] reported that the critical Reynolds number is in the range between 1700 and 1970, which is slightly lower than $Re = 2000$, at which Iwatsu *et al.* [14] obtained a pair of Taylor-Görtler-like (TGL) vortices in a cubic lid-driven cavity flow. Giannetti *et al.* obtained that cubic lid-driven cavity flow becomes unstable for Re just above 2000 via three-dimensional global linear stability analysis in [15]. Those aforementioned experimental and computational results suggest that there is a connection between oscillatory flows and TGL vortices.

In this article, we have studied numerically the transition from steady flow to oscillatory flow and occurrence of the TGL vortices in order to find out the relation between them if there is any. We have applied a first order accurate operator-splitting scheme, Lie's scheme [18], to the numerical solution of the Navier-Stokes equations, which is a continuation of the works discussed in [19] and [20]. The resulting methodology is easy to implement and quite modular since, for each time step, there is a sequence of three simpler subproblems needed to be solved. For the first subproblem we have used a L^2 -projection Stokes solver à la Uzawa to force the incompressibility condition. To solve the advection problem as the second subproblem, we have applied a wave-like equation method [21]. The third one is a diffusion problem which can be solved easily. The numerical results obtained for $Re = 400, 1000$ and 3200 show a good agreement with available numerical and experimental results in literature. Our simulation results predict that the critical Re_{cr} for the transition from steady flow to oscillatory (a Hopf bifurcation) is somewhere in $(1870, 1875)$ (resp., $(1860, 1865)$) for $h = 1/96$ (resp., $h = 1/60$). For the connection between the occurrence of TGL vortices and the transition from steady flow to oscillatory flow, we have investigated the flow field at Re close to Re_{cr} . The difference of flow fields at different instants of time shows a pair of vortices reminiscent of the GTL ones, but with much smaller magnitude for Re slightly smaller than Re_{cr} . For Re slightly larger than Re_{cr} , this flow field distortion is visible and then invisible periodically as a pair of TGL vortices. When increasing Re even higher (but $\downarrow 2000$), two tertiary vortices next to the corner vortices (one from each corner) start interacting with this pair periodically and the number of TGL pairs varies between one and two. All these pairs are symmetric. Thus our computational results suggest that the first pair of symmetric TGL vortices for $Re \downarrow 2000$ is actually the first oscillating mode flow, which exists all the way through the transition. The outline of this paper is as follows: We first introduce the formulation of the problem and then numerical method briefly in Section 2. In Section 3, the numerical results obtained for the classical lid-driven cavity flow problem at $Re = 400, 1000$, and 3200 are compared with numerical and experimental results for validation purpose. Then the critical Reynolds number for the transition from steady flow to oscillatory flow has been investigated in Section 4. Finally, the connection between oscillatory flow and TGL vortices has been studied in Section 5.

2 Formulation of the problem.

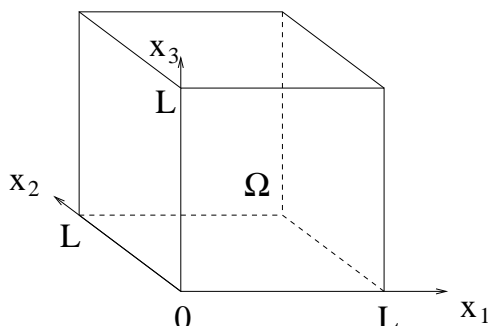


Figure 1: The computation domain Ω and coordinate system.

The governing equations for modeling incompressible viscous fluid flow in $\Omega \subset \mathbb{R}^3$ (see Fig. 1) for $T > 0$ are the Navier-Stokes equations, namely

$$\frac{\partial \mathbf{u}}{\partial t} - \nu \Delta \mathbf{u} + (\mathbf{u} \cdot \nabla) \mathbf{u} + \nabla p = \mathbf{f} \text{ in } \Omega \times (0, T), \quad (2.1)$$

$$\nabla \cdot \mathbf{u} = 0 \text{ in } \Omega \times (0, T), \quad (2.2)$$

$$\mathbf{u}(0) = \mathbf{u}_0, \text{ with } \nabla \cdot \mathbf{u}_0 = 0, \quad (2.3)$$

$$\mathbf{u} = \mathbf{u}_B(\mathbf{x}) \text{ on } \partial\Omega \times (0, T) \text{ with } \int_{\partial\Omega} \mathbf{u}_B \cdot \mathbf{n} d\Gamma = 0 \text{ on } (0, T), \quad (2.4)$$

where \mathbf{u} and p are the flow velocity and pressure, respectively, $\nu (= 1/Re)$ is a viscosity coefficient, \mathbf{f} is the body force, $\mathbf{u}_B(\mathbf{x})$ is the boundary condition, and \mathbf{n} is the unit outward normal vector at $\Gamma = \partial\Omega$. We denote by $v(t)$ the function $\mathbf{x} \rightarrow v(\mathbf{x}, t)$, \mathbf{x} being the generic point of \mathbb{R}^3 .

The numerical solution of problem (2.1)-(2.4) has generated a most abundant literature. Following Chorin [25, 26] and Temam [27, 28], most “modern” Navier-Stokes solvers are based on operator splitting algorithms (see, e.g., refs. [30], [31], [32] (Chapter 3) and [21] (Chapters 2 and 7)) in order to force the incompressibility condition via either H^1 -projection or L^2 -projection Stokes solver method. Among those methods for the numerical solution of (2.1)-(2.4), we have chosen the Lie scheme (see, e.g., see [21] and [8] for a general discussion of that scheme). It is first order accurate in time; but its low order accuracy in time is compensated by its modular, easy implementation, good stability, and robustness properties. To speed up the numerical solution of the cubic lid-driven cavity flow problem, we have time-discretized the related problem (2.1)-(2.4), using a three stage Lie scheme scheme, namely: (i) using a L^2 -projection Stokes solver à la Uzawa to force the incompressibility condition, (ii) an advection step, and (iii) a diffusion step. The resulting methodology reads as follows:

$$\mathbf{u}^0 = \mathbf{u}_0. \quad (2.5)$$

For $n \geq 0$, $\mathbf{u}^n \rightarrow \{\mathbf{u}^{n+1/3}, p^{n+1}\} \rightarrow \mathbf{u}^{n+2/3} \rightarrow \mathbf{u}^{n+1}$ via the solution of:

$$\begin{cases} \rho \frac{\mathbf{u}^{n+1/3} - \mathbf{u}^n}{\Delta t} + \nabla p^{n+1} = \mathbf{0} \text{ in } \Omega, \\ \nabla \cdot \mathbf{u}^{n+1/3} = 0 \text{ in } \Omega, \\ \mathbf{u}^{n+1/3} \cdot \mathbf{n} = 0 \text{ on } \Gamma, \end{cases} \quad (2.6)$$

$$\begin{cases} \frac{\partial \mathbf{w}}{\partial t} + (\mathbf{u}^{n+1/3} \cdot \nabla) \mathbf{w} = \mathbf{0} \text{ in } \Omega \times (t^n, t^{n+1}), \\ \mathbf{w}(t^n) = \mathbf{u}^{n+1/3}, \\ \mathbf{w}(t) = \mathbf{u}_B(\mathbf{x}) \text{ on } \Gamma_-^{n+1} \times (t^n, t^{n+1}), \end{cases} \quad (2.7)$$

$$\mathbf{u}^{n+2/3} = \mathbf{w}(t^{n+1}), \quad (2.8)$$

$$\begin{cases} \rho \frac{\mathbf{u}^{n+1} - \mathbf{u}^{n+2/3}}{\Delta t} - \mu \nabla^2 \mathbf{u}^{n+1} = \mathbf{f}^{n+1} \text{ in } \Omega, \\ \mathbf{u}^{n+1} = \mathbf{u}_B(\mathbf{x}) \text{ on } \Gamma. \end{cases} \quad (2.9)$$

Two simplifications take place for the lid-driven cavity flow problem considered here: namely, $\mathbf{f} = \mathbf{0}$ and $\Gamma_-^{n+1} = \{\mathbf{x} | \mathbf{x} \in \Gamma, \mathbf{u}_B(\mathbf{x}) \cdot \mathbf{n}(\mathbf{x}) < 0\} = \emptyset$.

For the space discretization, we have used, as in [21] (Chapter 5) and [29], a P_1 -*iso*- P_2 (resp., P_1) finite element approximation for the velocity field (resp., pressure) defined on uniform tetrahedral meshes \mathcal{T}_h (resp., \mathcal{T}_{2h}). The problem (2.6) is reminiscent of those encountered when applying Chorin's projection method ([25]). Three subproblems in (2.6)-(2.9) are very classical problems and each one can be solved by many different available methods. This is the key point of the operator splitting methods. The saddle point problem (2.6) has been solved by a Uzawa/preconditioned conjugate gradient algorithm as discussed in [21] (Section 21). Problem (2.7)-(2.8) has been solved by a wave-like equation method (e.g., see [35] and [21] (Section 31)) which does not introduce numerical dissipation, unlike the commonly used *upwinding* schemes. The problem (2.9) is a classical discrete elliptic problem which can be solved easily.

3 Numerical Results

For the lid-driven cavity flow problem in a cube, considered here, we took $\Omega = (0, 1)^3$ as computational domain and defined the Dirichlet data \mathbf{u}_B by

$$\mathbf{u}_B(\mathbf{x}) = \begin{cases} (1, 0, 0)^T \text{ on } \{\mathbf{x} | \mathbf{x} = (x_1, x_2, 1)^T, 0 < x_1, x_2 < 1\}, \\ \mathbf{0} \text{ elsewhere on } \Gamma. \end{cases} \quad (3.1)$$

We considered that the steady state has been reached when the change between two consecutive time step in the simulation, $\|\mathbf{u}_h^n - \mathbf{u}_h^{n-1}\|_\infty / \Delta t$, is less than 10^{-4} , and then took \mathbf{u}_h^n as the steady state solution.

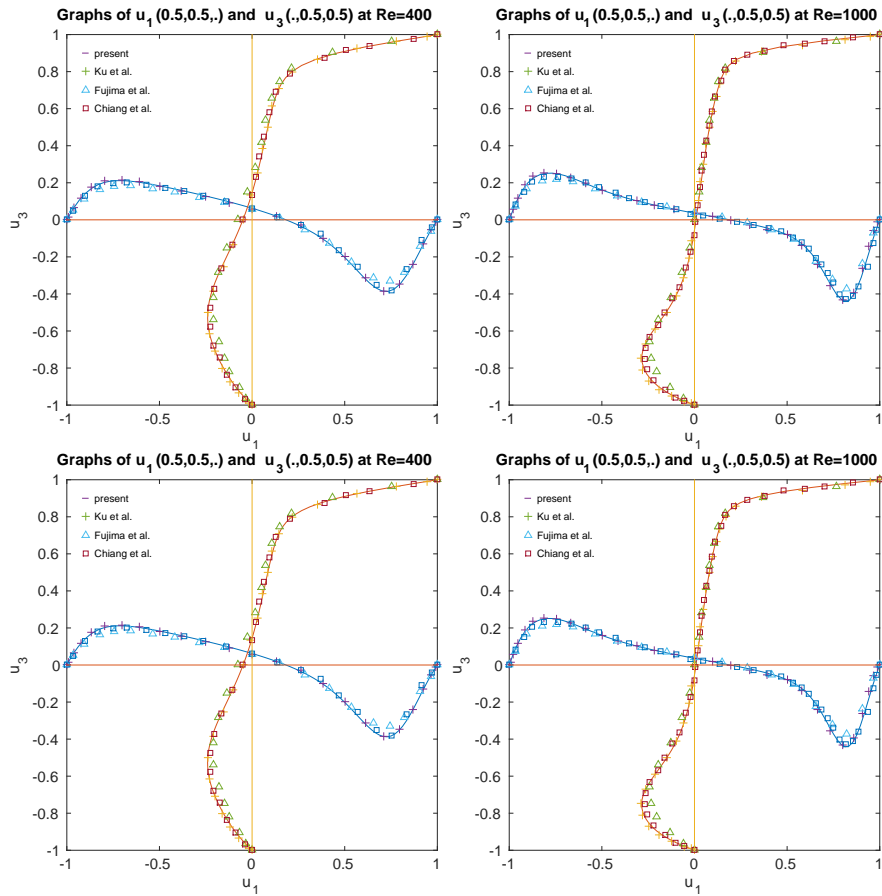


Figure 2: Comparisons of the numerical results obtained for $h = 1/60$ (top) and $1/96$ (bottom) at $Re=400$ (left) and 1000 (right).

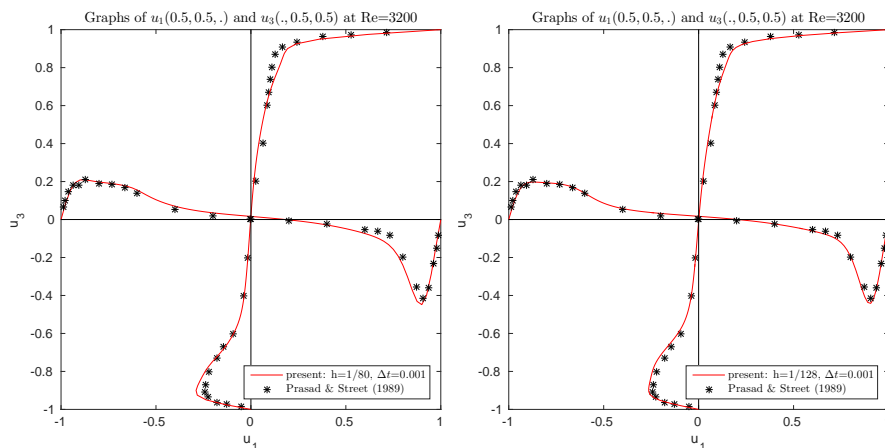


Figure 3: Comparisons of the numerical results at $Re=3200$ obtained for $h = 1/80$ and $220 \leq t \leq 400$ (left) and for $h = 1/128$ and $158 \leq t \leq 278$ (right).

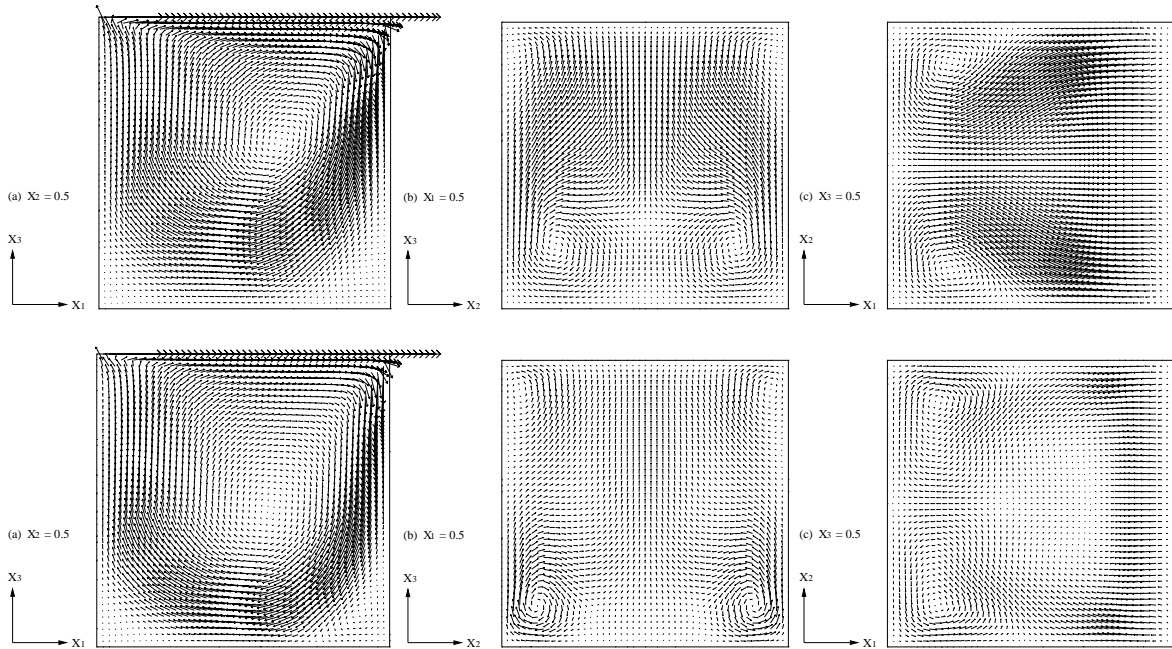


Figure 4: Velocity vector of steady flow for $Re=400$ (top) and 1000 (bottom) projected on the planes $x_2 = 0.5$ (left), $x_1 = 0.5$ (middle), and $x_3 = 0.5$ (right) for $h = 1/96$ and $\Delta t=0.001$. The vector scale in the middle and right plots is twice that of the actual size.

3.1 Validation

To validate the numerical methodology, we have considered for the velocity mesh size the values $h = 1/60$ and $1/96$ associated with the time step $\Delta t=0.001$. For $Re=400$ and 1000 , the results reported in Figure 2 show a very good agreement with those obtained in [22], [23] and [24]. Velocity vectors of steady flows obtained for $Re=400$ and 1000 are shown in Figure 4. Those velocity field vectors are projected orthogonally to the three planes, $x_2 = 0.5$, $x_1 = 0.5$, and $x_3 = 0.5$, and the length of the vectors has been doubled in the two later planes to observe the flow more clearly. The plots show that the center of the primary vortex moves down as the Reynolds increases from 400 to 1000 and secondary vortices appear in two lower corners, which is similar, in some sense, to what happens for the two-dimensional wall-driven cavity flow. At $x_1 = 0.5$, a pair of secondary vortices moves toward the lower corners when the Reynolds increases. Also another pair of vortices appears at the top corners. At $x_3 = 0.5$, there is a pair of secondary vortices near the upstream wall.

Another validation has been done at $Re=3200$ for $h = 1/80$ and $1/128$ and $\Delta t=0.001$. For $Re=3200$ in a cubic cavity, experiments [36] indicates that there are usually two pairs of TGL vortices. Moreover, these vortices are not stationary; they meander to and fro over the bottom wall closer to the end wall in the spanwise direction. In [37] and [38], the number of pairs of TGL vortices obtained numerically varies between two and three. Figure 3 shows the averaged speed profiles $u_1(0.5, 0.5, \cdot)$ and $u_1(\cdot, 0.5, 0.5)$ are in a good agreement with the

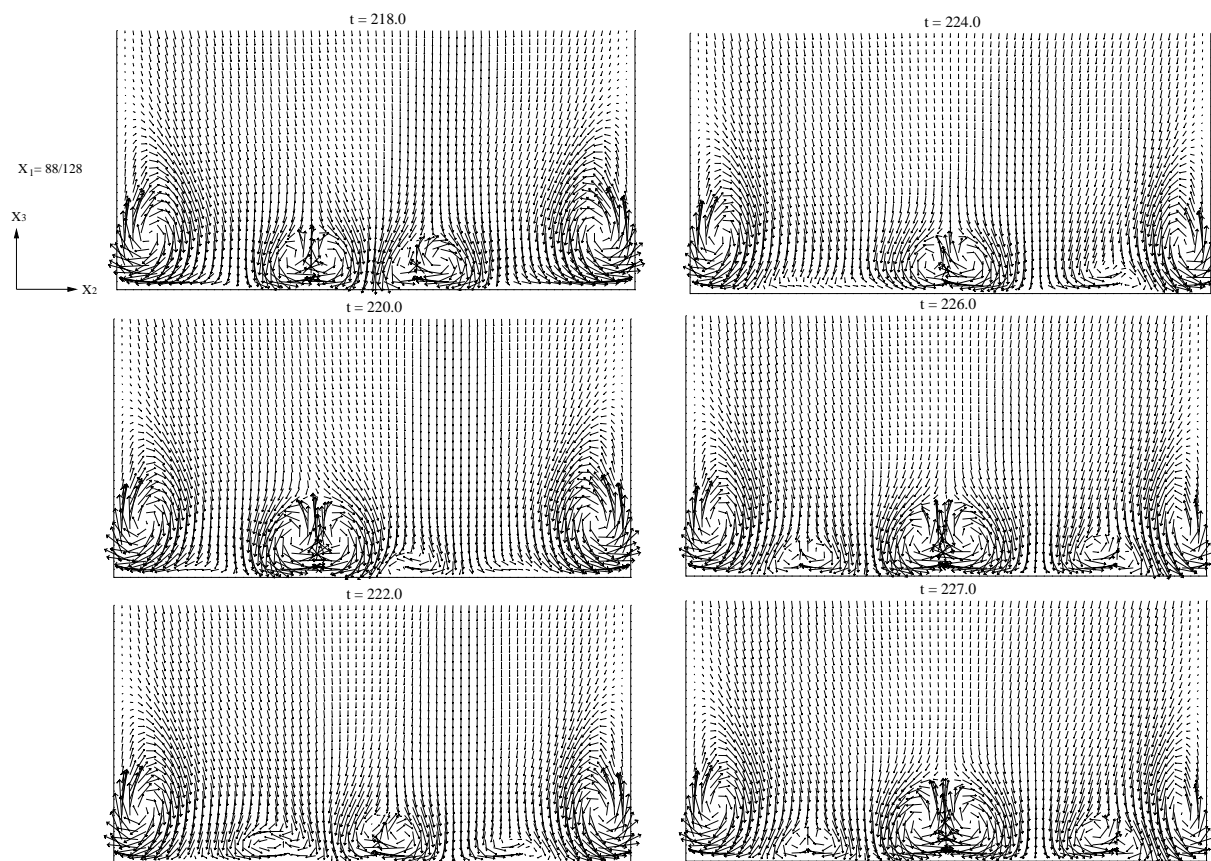


Figure 5: Projected velocity vectors on $x_1 = 88/128$ for $Re = 3200$ at different instants of time shows interaction between TGL vortices and corner vortices. The scale of vectors is twice that of the actual one.

experimental values obtained in [36]. Our simulation results show two to three pairs of TGL vortices at $Re = 3200$ in Figure 5. For $218 \leq t \leq 220$, two pairs of TGL vortices interact with each other and corner vortices and one pair of TGL vortices is diminished later. Then another two pairs of TGL vortices gradually show up for $222 \leq t \leq 227$.

3.2 Transition from steady flow to oscillatory flow

A documented feature of three-dimensional lid-driven cavity flows is that they may exhibit Taylor-Görtler-like (TGL) vortices if Re is sufficiently large. In this section, we focus on the transition from steady flow to oscillatory flow and TGL vortices for the Reynolds number Re just below 2000. Indeed, Iwatsu *et al.* [14] obtained a pair of Taylor-Görtler-like (TGL) vortices at $Re = 2000$. Also as predicted in [11] and [12], a transition from steady flow to oscillatory flow occurs at $Re_{cr} < 2000$. On the other hand, using a global linear stability analysis, Gianetti *et al.* found (ref. [15]) that cubic lid-driven cavity flow becomes unstable

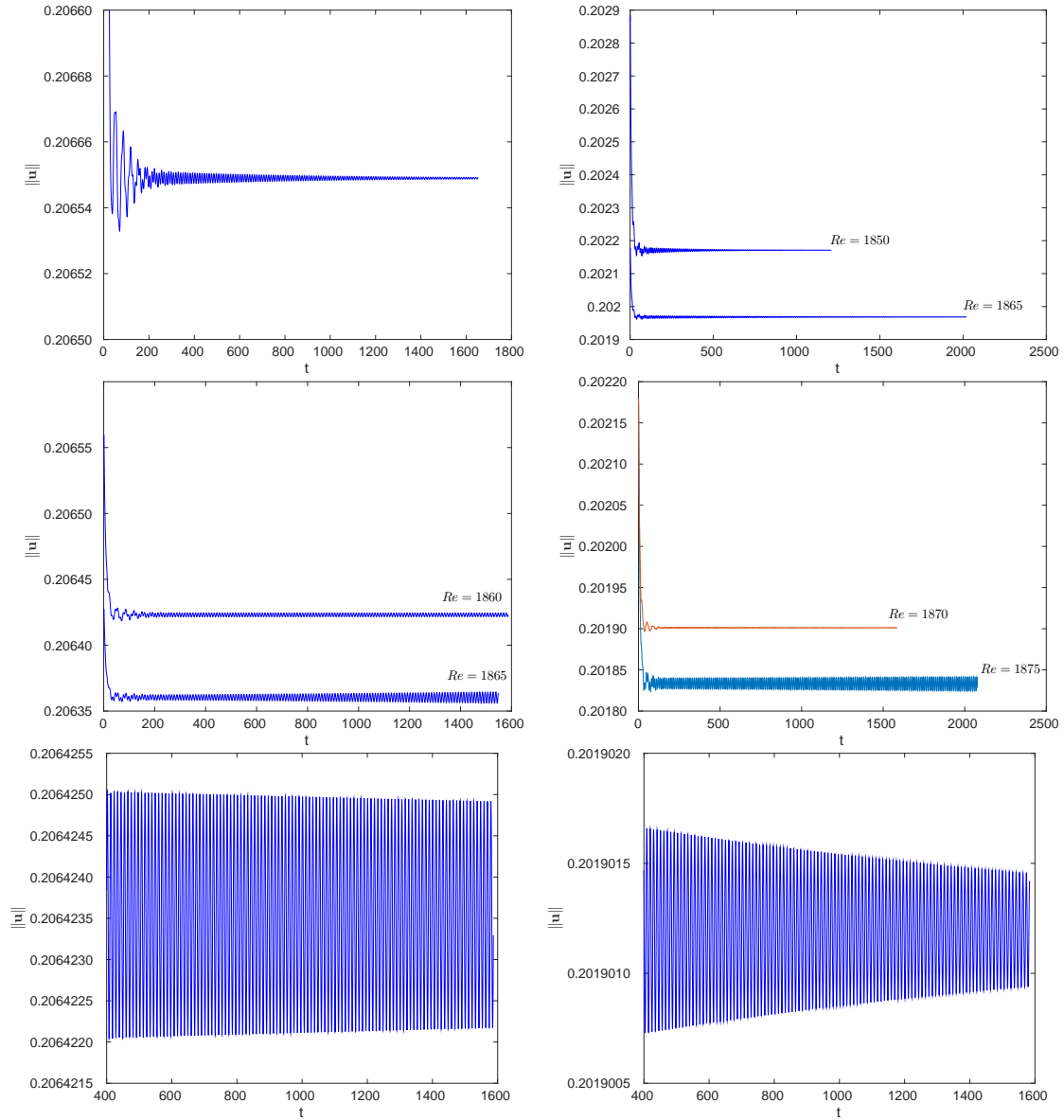


Figure 6: Histories of the flow field L^2 -norm for $h = 1/60$ (left) and $1/96$ (right): (a) $Re = 1850$ (top left), $Re = 1860$ and 1865 (middle left) and an enlargement of the case of $Re = 1860$ (bottom left); (b) $Re = 1850$ and 1865 (top right), $Re = 1870$ and 1875 (middle right) and an enlargement of the case of $Re = 1870$ (bottom right).

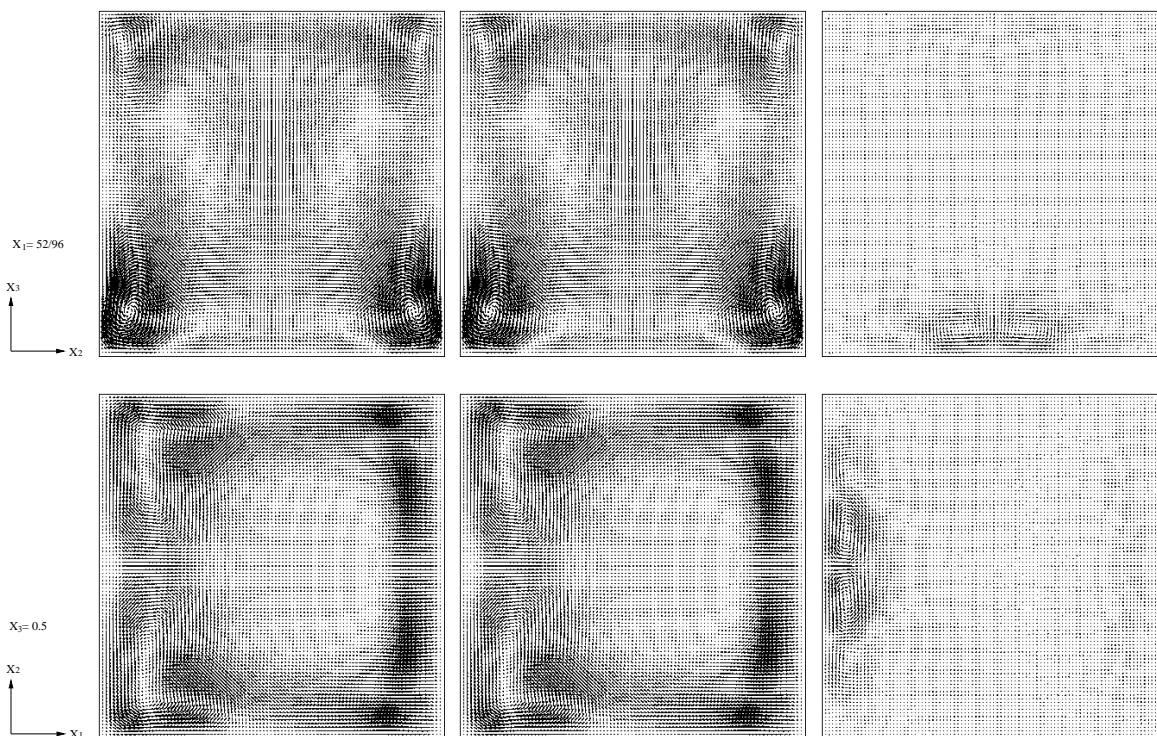


Figure 7: Left and middle: Projections (at $Re = 1870$) of the cavity flow velocity vector fields associated with the peak (left) and bottom (middle) of the velocity L^2 -norm during an oscillation. Right: Projections (at $Re = 1870$) of the vector field obtained by difference of the velocity vector fields associated with the peak and bottom of the velocity L^2 -norm. All the vector fields are projected on the planes $x_1 = 52/96$ (top) and $x_3 = 0.5$ (bottom). The vector scale for the field obtained by difference (right) is 500 times that of the actual one, while the scale for the two other fields (left and middle) is twice that of the actual one.

for Re just above 2000. All these results (ours in particular) lead us to suspect that the Hopf bifurcation is connected to the TGL vortices at Re slightly below 2000.

To study the transition from steady flow to oscillatory flow, we have analyzed the history of the L^2 -norm of the flow field, $\|\mathbf{u}_h^n\|$, for different values of Re and of the mesh size h . For $h = 1/60$, the flow field evolves to steady state for $Re \leq 1860$ and the amplitude of the oscillation of the flow field L^2 -norm decreases also in time. At $Re = 1865$, the steady state criterion is not satisfied and the amplitude of the oscillation increases in time as in Figure 6. Thus we conclude that the critical Reynolds number Re_{cr} for the occurrence of the transition is somewhere between 1860 and 1865. The frequencies of the flow field L^2 -norm oscillation are 0.09449 and 0.09456 for $h = 1/60$ at $Re = 1860$ and 1865, respectively. Applying a similar analysis, Re_{cr} is in $(1870, 1875)$ for $h = 1/96$ and the associated histories of the flow field L^2 -norm being shown in Figure 6. The frequencies of the L^2 -norm oscillation are 0.095147 and 0.095057 for $h = 1/96$ at $Re = 1870$ and 1875, respectively.

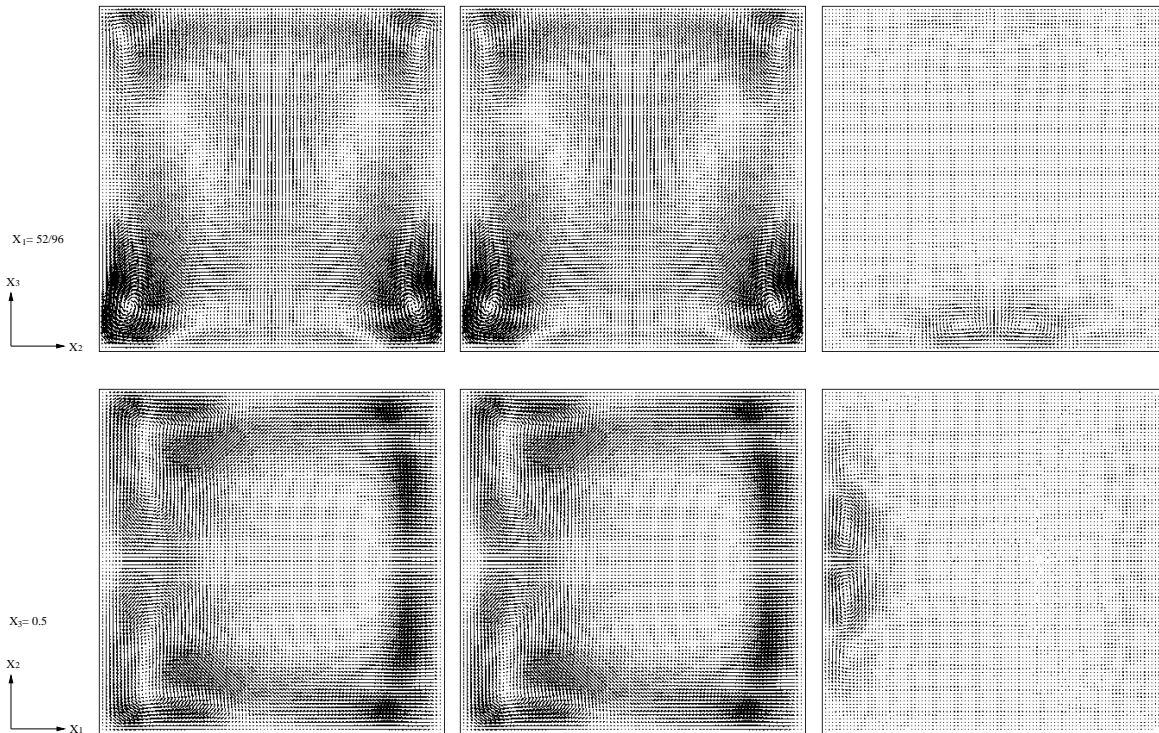


Figure 8: Left and middle: Projections (at $Re = 1875$) of the cavity flow velocity vector fields associated with the peak (left) and bottom (middle) of the velocity L^2 -norm during an oscillation. Right: Projections (at $Re = 1875$) of the vector field obtained by difference of the velocity vector fields associated with the peak and bottom of the velocity L^2 -norm. All the vector fields are projected on the planes $x_1 = 52/96$ (top) and $x_3 = 0.5$ (bottom). The vector scale for the field obtained by difference (right) is 15 times that of the actual one, while the scale for the two other fields (left and middle) is twice that of the actual one.

The pictures of Figure 6 show oscillations of the flow field L^2 -norm and the oscillation amplitude either decreases or increases in time depending on Re . These oscillations indicate that there is a periodic flow field distortion. In order to investigate the computed flow distortion, we have visualized in Figures 7 (for $Re=1870$) and 8 (for $Re=1875$) the velocity fields for $h = 1/96$ associated with the peak and bottom of the velocity field L^2 -norm, and the vector field associated with the difference of the above two velocity fields. The top (resp., bottom) pictures have been obtained by projecting the vector fields on the plane $x_1 = 52/96$ (resp., $x_3 = 1/2$). Figures 7 and 8 show no evidence of TGL vortices for the velocity fields computed with $h = 1/96$ at $Re=1870$ and 1875 ; however, the pictures on the right of Figures 7 and 8, obtained by the vector field difference detailed above, show a pair of vortices reminiscent of the GTL ones with much smaller magnitude. Those vector fields have been amplified by a factor of 500 (resp., 15) for $Re=1870$ (resp., 1875) in order to make them visible. For $h = 1/60$, we have obtained similar results for $Re=1860$ and 1865 . This vortex pair keeps hiding there and becomes stronger as Re increases. These

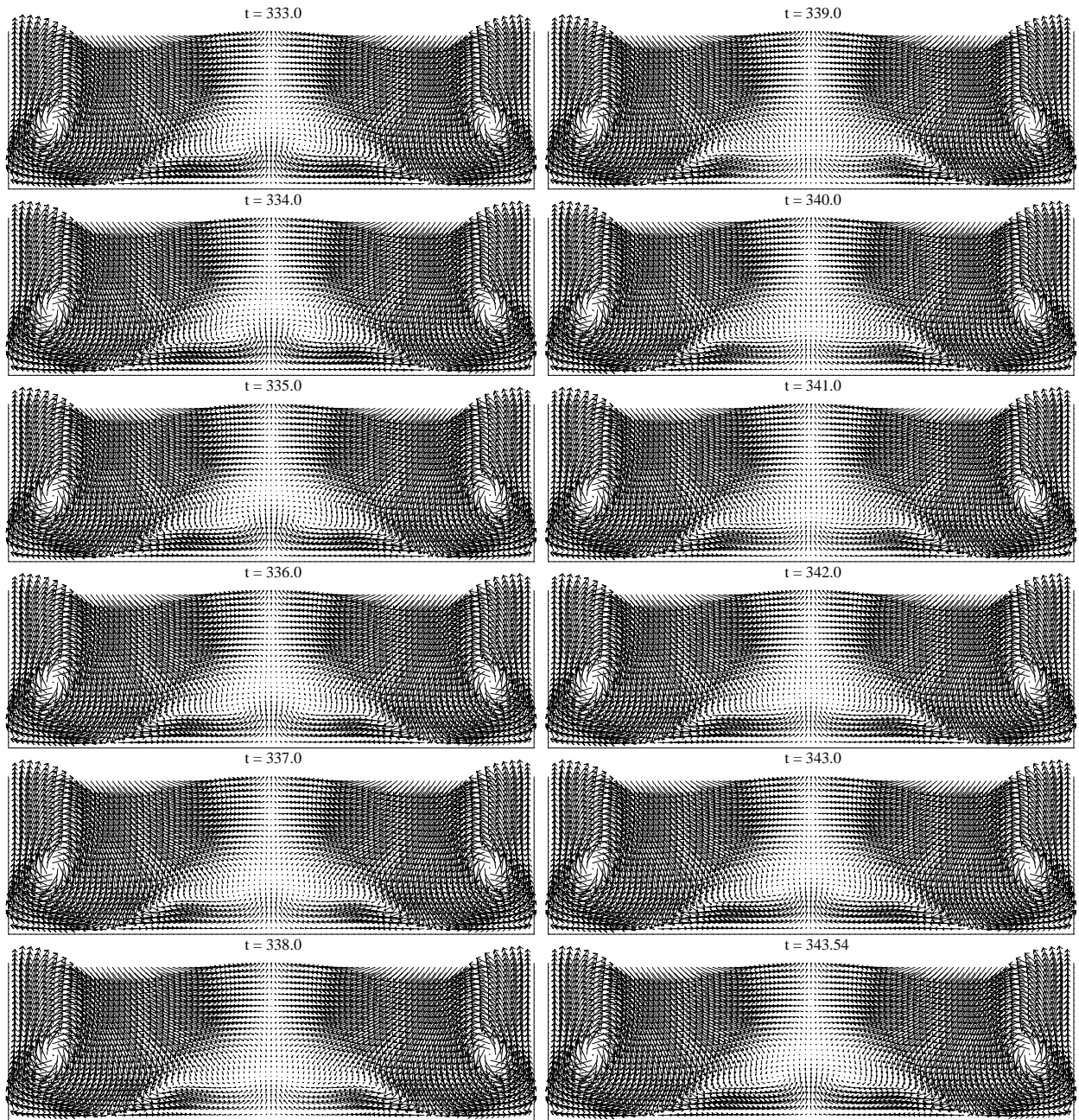


Figure 9: Projected velocity vector field of the cavity flow at $Re=1885$ on the plane $x_1 = 54/96$ at different instants of time during one oscillation of the flow field L^2 -norm from $t = 333$ to 343.54 (for enhancing the visibility of the TGL vortices we proceeded as follows: (i) for those projected vectors of length ≤ 0.02 the vector scale is 10 times that of the actual one and (ii) for those projected vectors of length > 0.02 , the length is reduced to 0.02 first and then plotted as in (i)).

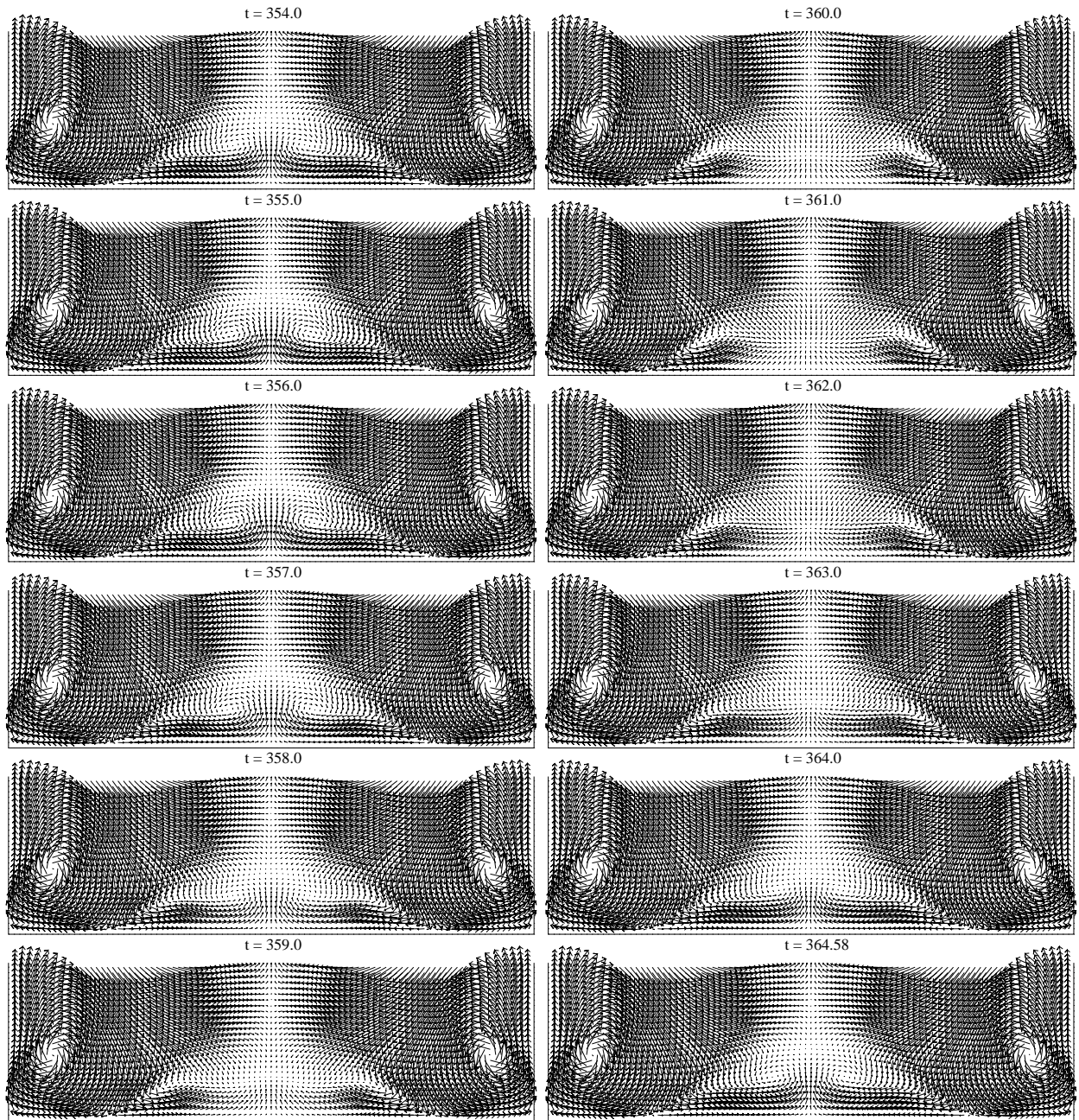


Figure 10: Projected velocity vector field of the cavity flow at $Re=1900$ on the plane $x_1 = 54/96$ at different instants of time during one oscillation of the flow field L^2 -norm from $t = 354$ to 364.58 (for enhancing the visibility of the TGL vortices we proceeded as follows: (i) for those projected vectors of length ≤ 0.02 the vector scale is 10 times that of the actual one and (ii) for those projected vectors of length > 0.02 , the length is reduced to 0.02 first and then plotted as in (i)).

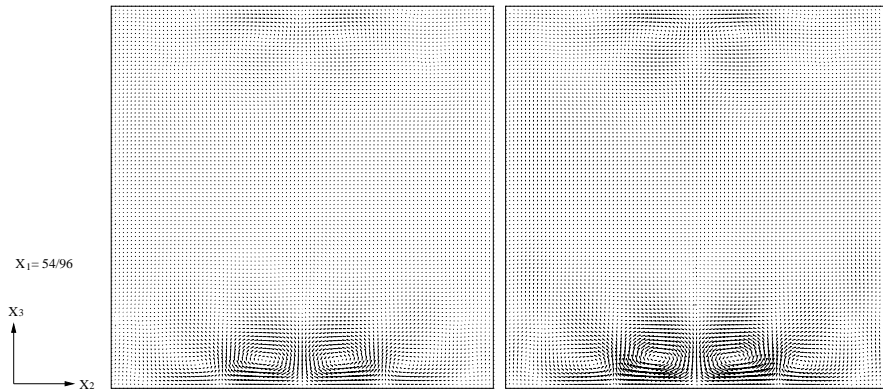


Figure 11: Projected velocity vector field of the difference of the velocity fields at $t = 340$ and $t = 342$ on the plane $x_1 = 54/96$ for $Re=1885$ (left) and that of the difference of the velocity fields at $t = 361$ and $t = 363$ on the plane $x_1 = 54/96$ for $Re=1900$ (right). The vector scale is 25 times that of the actual one for both.

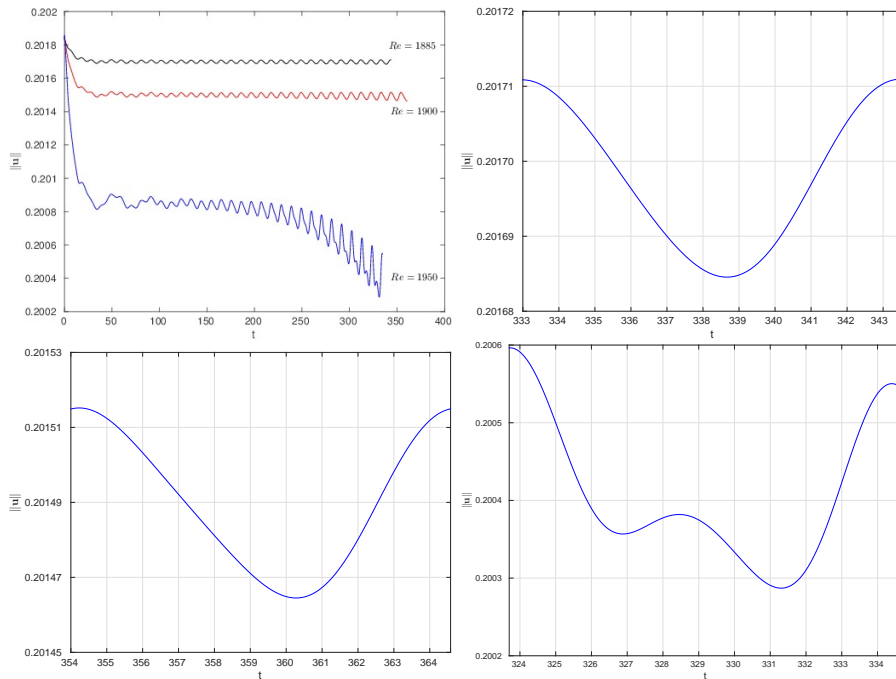


Figure 12: Histories of the flow field L^2 -norm for $h = 1/96$ at $Re=1885$, 1900 , and 1950 (top left) and one oscillation of the flow field L^2 -norm for $Re=1885$ (top right), $Re=1900$ (bottom left), and $Re=1950$ (bottom right).

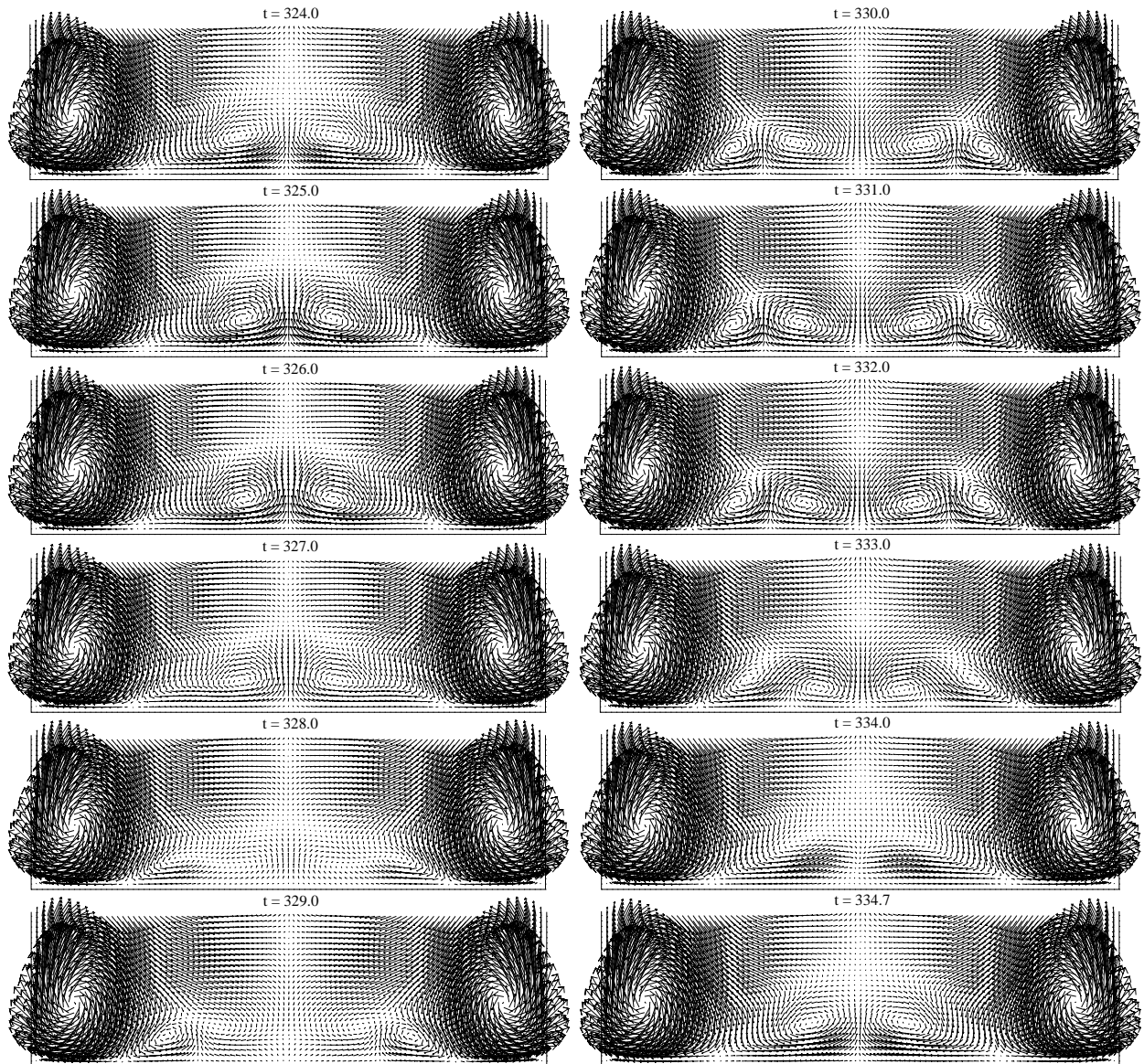


Figure 13: Projected velocity field vector of the cavity flow for $Re=1950$ on the plane $x_1 = 54/96$ at different instants of time during one oscillation of the flow field L^2 -norm from $t = 324$ to 334.7 . The vector scale is 5 times that of the actual one for both.

results suggest that the TGL vortices observed for Re slightly below 2000 are related to the onset of an oscillatory flow. Thus we have further studied the oscillatory flow at $Re=1885$, 1900, and 1950. At $Re=1885$, a pair of TGL vortices becomes visible. In Figure 9, we have visualized (using a nonlinear scaling to enhance visibility) several snap-shots of the velocity field during an oscillation time period. A pair of TGL vortices is being formed in the time interval $[333, 336]$ and then this pairs of TGL vortices disappear after $t = 337$; finally they reappear during the next time-period (at $t = 343.54$). This pair of TGL vortices is stationary and remains symmetric with respect to the mid-plane $x_2 = 1/2$. Actually this pair of TGL vortices for $333 \leq t \leq 336$ does occur from the peak of the flow field L^2 -norm to the middle between the peak and the bottom as shown in Figure 12. Then there is no significant sign of TGL vortices at the bottom of the flow field L^2 -norm for $337 \leq t \leq 342$. But in Figure 11, there is a vortex pair in the flow field distortion obtained by difference of the velocity flow fields at $t = 340$ and $t = 342$, which is reminiscent of those visualized on the right of Figures 7 and 8. At $Re=1900$, we have also obtained numerical results similar to those for $Re=1885$ (see Figures 11, 10 and 12). In the histories of the flow field L^2 -norm for $Re=1885$ and 1900 shown in Figure 12, there is a dominated single mode which corresponds to the appearance of TGL vortices discussed above. When increasing Re to 1950, there is a second mode gradually showing up in time. In the snapshots of velocity field projected on the plane $x_1 = 54/96$ for one oscillation of the flow field L^2 -norm (see Figures 12 and 13), the pair of TGL vortices (like those the dominated modes for $Re=1885$ and 1900) again occurs from the peak to the first bottom (for $324 \leq t \leq 327$). But for $329 \leq t \leq 333$, a tertiary vortex next to the corner vortex appears, interacts with the symmetric one, and disappear; finally the symmetric pair show up again to start another period. These results support that the TGL vortices observed for Re slightly below 2000 are related to the oscillatory flows.

4 Conclusion

In this article, we have studied numerically the transition from steady flow to oscillatory flow and occurrence of the TGL vortices via a three-stage Lie's scheme. The numerical results obtained for $Re=400$, 1000 and 3200 show a good agreement with available numerical and experimental results in literature. Our simulation results predict that the critical Re_{cr} for the transition from steady flow to oscillatory (a Hopf bifurcation) is somewhere in (1870, 1875) (resp., (1860, 1865)) for $h = 1/96$ (resp., $h = 1/60$). For the connection between the occurrence of TGL vortices and the transition from steady flow to oscillatory flow, we have investigated the flow field at Re close to Re_{cr} . The difference of flow fields at different instants of time shows a pair of vortices reminiscent of the GTL ones, but with much smaller magnitude for Re slightly smaller than Re_{cr} . For Re slightly larger than Re_{cr} , this flow field distortion is visible and then invisible periodically as a pair of TGL vortices. When increasing Re to 1950, two tertiary vortices next to the corner vortices (one from each corner) start interacting with this pair periodically and the number of TGL pairs varies between one and two. All these pairs are symmetric. Thus our computational results suggest that the first pair of symmetric TGL vortices for $Re \downarrow 2000$ is actually the first oscillating mode flow,

which exists all the way through the transition.

Acknowledgments.

We acknowledge also the support of NSF (grant DMS-1418308).

References

- [1] C.K. Aidun, N.G. Triantafillopoulos and J.D. Benson. Global stability of a lid-driven cavity with throughflow: Flow visualization studies. *Phys. Fluids A*, **3** (1991), 2081-2091.
- [2] P.N. Shankar and M.D. Deshpande. Fluid mechanics in the driven cavity. *Annu. Rev. Fluid Mech.*, **32** (2000), 93-136.
- [3] R. Iwatsu, K. Ishii, T. Kawamura, K. Kuwahara and J.M. Hyun. Numerical simulation of three-dimensional flow structure in a driven cavity. *Fluid Dyn. Res.*, **5** (1989), 173-189.
- [4] J. Shen. Hopf bifurcation of the unsteady regularized driven cavity flow. *J. Comp. Phys.*, **95** (1991), 228-245.
- [5] O. Goyon. High-Reynolds number solutions of Navier-Stokes equations using incremental unknowns. *Comput. Methods Appl. Mech. Engrg.*, **130** (1996), 319-335.
- [6] F. Auteri, N. Parolini and L. Quartapelle. Numerical investigation on the stability of singular driven cavity flow. *J. Comput. Phys.*, **183** (2002), 1-25.
- [7] M. Sahin and R.G. Owens. A novel fully implicit finite volume method applied to the lid-driven cavity problem. Part II: Linear stability analysis. *Int. J. Numer. Meth. Fluids*, **42** (2003), 79-88.
- [8] R. Glowinski, S. Osher, W. Yin, W. (eds.): *Operator-Splitting Methods for Communications and Imaging*, Science and Engineering. Springer (to appear).
- [9] C.H. Bruneau and M. Saad. The 2D lid-driven cavity problem revisited. *Computers & Fluids*, **35** (2006), 326-348.
- [10] T. Wang, T.-W. Pan and R. Glowinski. A comparison of L^2 -projection and H^1 -projection methods for the numerical simulation of incompressible viscous fluid flow: A case study. *Chinese Journal of Engineering Mathematics*, **25** (2008), 761-778.
- [11] Y. Feldman and A.Y. Gelfgat. Oscillatory instability of a three-dimensional lid-driven flow in a cube. *Phys. Fluids*, **22** (2010), 093602.

- [12] A. Liberzon, Y. Feldman, and A.Y. Gelfgat. Experimental observation of the steady-oscillatory transition in a cubic lid-driven cavity. *Phys. Fluids*, **23** (2011), 084106.
- [13] K. Anupindi, W. Lai, and S. Frankel. Characterization of oscillatory instability in lid driven cavity flows using lattice Boltzmann method. *Computers & fluids*, **92** (2014), 7-21.
- [14] R. Iwatsu, J.M. Hyun and K. Kuwahara. analyses of three-dimensional flow calculations in a driven cavity. *Fluid Dyn. Res.*, **6** (1990), 91-102.
- [15] F. Giannetti, P. Luchini and L. Marino. Linear stability analysis of three-dimensional lid-driven cavity flow. In *Atti del XIX Congresso AIMETA di Meccanica Teorica e Applicata*, pp. 14-17. Aras Edizioni Ancona, Italy, 2009.
- [16] J. R. Koseff and R. L. Street. Visualization studies of a shear driven three-dimensional recirculating flow. *J. Fluids Eng.*, **106** (1984), 21-29.
- [17] J. R. Koseff and R. L. Street. The lid-driven cavity flow: a synthesis of qualitative and quantitative observations. *J. Fluids Eng.*, **106** (1984), 390-398.
- [18] A.J. Chorin, T.J.R. Hughes, M.F. McCracken and J.E. Marsden. Product formulas and numerical algorithms. *Comm. Pure Appl. Math*, **31** (1978), 205-256.
- [19] T.-W. Pan and R. Glowinski. A projection/wave-like equation method for the numerical simulation of incompressible viscous fluid flow modeled by the Navier-Stokes equations. *Computational Fluid Dynamics Journal*, **9** (2009), 28-42.
- [20] T. Wang, T.-W. Pan and R. Glowinski. A comparison of L^2 -projection and H^1 -projection methods for the numerical simulation of incompressible viscous fluid flow: A case study. *Chinese Journal of Engineering Mathematics*, **25** (2008), 761-778.
- [21] R. Glowinski. Finite element methods for incompressible viscous flow. *Handbook of Numerical Analysis*, P.G. Ciarlet, J.-L. Lions eds., Vol. IX, pp. 3-1976. North-Holland, Amsterdam, 2003.
- [22] S. Fujima, M. Tabata and Y. Fukasawa. Extension to three-dimensional problems of the upwind finite element scheme based on the choice up- and downwind points. *Comp. Meth. Appl. Mech. Eng.*, **112** (1994), 109-131.
- [23] H.C. Ku, R.S. Hirsh and T.D. Taylor. A pseudospectral method for solution of the three-dimensional incompressible Navier-Stokes equations. *J. Comp. Phys.*, **70** (1987), 439-462.
- [24] T.P. Chiang, W.H. Sheu and R.R. Hwang. Effect of Reynolds number on the eddy structure in a lid-driven cavity. *Int. J. Numer. Meth. Fluids*, **26** (1998), 557-579.
- [25] A.J. Chorin. A numerical method for solving incompressible viscous flow problems. *J. Comput. Phys.*, **2** (1967), 12-26.

- [26] A.J. Chorin. Numerical solution of the Navier-Stokes equations. *Math. Comput.*, **23** (1968), 341-354.
- [27] R. Temam. Sur l'approximation des équations de Navier-Stokes par la méthode des pas fractionnaires (I). *Arch. Rat. Mech. Anal.*, **32** (1969), 135-153.
- [28] R. Temam. Sur l'approximation des équations de Navier-Stokes par la méthode des pas fractionnaires (II). *Arch. Rat. Mech. Anal.*, **33** (1969), 377-385.
- [29] M.O. Bristeau, R. Glowinski and J. Periaux. Numerical methods for the Navier-Stokes equations. Applications to the simulation of compressible and incompressible viscous flow. *Computer Physics Reports*, **6** (1987), 73-187.
- [30] G.I. Marchuk. Splitting and alternate direction methods. *Handbook of Numerical Analysis*, P.G. Ciarlet, J.-L. Lions eds., Vol. I, pp. 197-462. North-Holland, Amsterdam, 1990.
- [31] S. Turek. A comparative study of time-stepping techniques for the incompressible Navier-Stokes equations: from fully implicit non-linear schemes to semi-implicit projection methods. *Int. J. Num. Math. Fluids*, **22** (1996), 987-1011.
- [32] M. Marion and R. Temam. Navier-Stokes Equations. *Handbook of Numerical Analysis*, P.G. Ciarlet, J.-L. Lions eds., Vol. VI, pp.503-689. North-Holland, Amsterdam, 1998.
- [33] R. Glowinski and O. Pironneau. Finite Element Methods for Navier-Stokes Equations. *Annu. Rev. Fluid Mech.*, **24** (1992), 167-204.
- [34] O. Pironneau. *Finite Element Methods for Fluids*. J. Wiley, Chichester, 1989.
- [35] E.J. Dean and R. Glowinski. A wave equation approach to the numerical solution of the Navier-Stokes equations for incompressible viscous flow. *C.R. Acad. Sci. Paris, Série I*, t. **325** (1997), 783-791.
- [36] A.K. Prasad and J.R. Koseff. Reynolds number and end-wall effects on a lid-driven cavity flow. *Phys. Fluids A*, **1** (1989), 208-218.
- [37] C.Y. Perng and R.L. Street. Threedimensional unsteady flow simulations: Alternative strategies for a volumeaveraged calculation. *Int. J. Num. Math. Fluids*, **9** (1989), 341-362.
- [38] C.M. Teixeira. Digital physics simulation of lid-driven cavity flow. *Int. J. Mod. Phys. C*, **8** (1997), 685-696.